INDERSCIENCE PUBLISHERS
Linking academia, business and industry through research

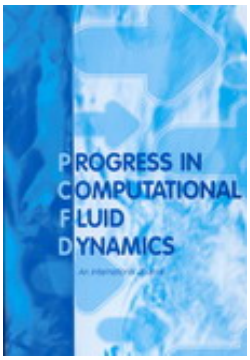

Progress in Computational Fluid Dynamics, An International Journal

ISSN online: 1741-5233 - ISSN print: 1468-4349
https://www.inderscience.com/pcfd

Study of the multi-size effect of bubbles in multiphase pump based on a coupled TFM-PBM model

Juping Zhou, Wei Han, Rennian Li, Diyi Chen

DOI: 10.1504/PCFD.2024.10067233

Article History:

Received:	02 August 2023
Last revised:	30 November 2023
Accepted:	01 December 2023
Published online:	06 January 2025

Study of the multi-size effect of bubbles in multiphase pump based on a coupled TFM-PBM model

Juping Zhou*

School of Energy and Power Engineering,
Lanzhou University of Technology,
Lanzhou, Gansu Province, 730050, China
Email: 221080704003@lut.edu.cn
*Corresponding author

Wei Han and Rennian Li

School of Energy and Power Engineering,
Lanzhou University of Technology,
Lanzhou, Gansu Province, 730050, China
and
Key Laboratory of Advanced Pumps,
Valves and Fluid Control System of the Ministry of Education,
Lanzhou University of Technology, China
Email: hanwei@lut.edu.cn
Email: lirn@lut.edu.cn

Diyi Chen

Department of Electrical Engineering,
College of Water Resources and Architectural Engineering,
Northwest Agriculture and Forestry University,
Yangling 712100, China
Email: diyichen@nwsuaf.edu.cn

Abstract: The coalescence and breakup of bubbles lead to variations in bubble diameter during the flow within the impeller. This study examines the characteristics of bubble size distribution and internal flow mechanisms in multiphase pumps under diverse operating conditions, employing the Eulerian-Eulerian two-fluid model (TFM) and the population balance model (PBM) for analysis. The results show that the main factor leading to gas-liquid phase separation is the pressure gradient force due to the high-density difference. The bubble coalescence frequency at the impeller hub is higher than the bubble breakup frequency with increasing inlet gas volume fraction (IGVF). The large bubbles begin predominating and become the primary cause of air plugging the impeller channel. Moreover, the capacity of the rotating liquid within the impeller to carry the gas improves with an escalating flow rate, impeding the coalescence of bubbles. This dynamic positively influences the gas-plugging behaviour in the channel.

Keywords: multiphase flow; TFM-PBM coupling model; pressure gradient; gas phase retention; air blocking phenomenon.

Reference to this paper should be made as follows: Zhou, J., Han, W., Li, R. and Chen, D. (2025) 'Study of the multi-size effect of bubbles in multiphase pump based on a coupled TFM-PBM model', *Progress in Computational Fluid Dynamics*, Vol. 25, No. 1, pp.44–53.

Biographical notes: Juping Zhou graduated from Lanzhou University of Technology in 2021 with a Bachelor's in Energy and Power Engineering, and is currently studying for a PhD in Fluid Mechanics and Engineering at Lanzhou University of Science and Technology. She is mainly engaged in the research of fluid mechanics and multiphase flow theory.

Wei Han received his PhD degree from Lanzhou University of Technology in 2009, and is currently a Professor and Doctoral Supervisor at the School of Energy and Power Engineering of Lanzhou University of Technology, engaged in the research of multiphase flow theory of fluid mechanics and the dynamic performance of pump jet propulsion.

Rennian Li graduated from Gansu University of Technology with a Master's degree in 1988, and has been a Professor and Doctoral Supervisor at Lanzhou University of Technology since 2000. He is engaged in the research of multiphase flow theory of fluid machinery and engineering, and the aerodynamic performance of wind turbine.

Diyi Chen is a Professor and Doctoral Supervisor from Northwest A&F University; from September 2008 to January 2009, Xi'an Jiaotong University, School of Electrical Engineering for further study, July 2012 to July 2013, he is a visiting scholar from Arizona State University, USA, and October 2015 to September 2016, he is a visiting scholars from Curtin University, Australia. He is mainly engaged in research on the stability and control of hydraulic machinery systems (pumping station and hydropower plant engineering).

1 Introduction

Oil and natural gas are pivotal in humankind's economic development and energy security (Wangxu et al., 2021; Li et al., 2023). In recent years, the world's proven oil and gas reserves have been growing with the development of technology. Still, people's demand for oil and gas is also increasing with the improvement in living standards. Therefore, it is exceptionally critical for the continuous development and further enhancement of the technological means of oil and gas exploration, extraction, and transportation. The helical-axial multiphase pump is a crucial piece of equipment in long-distance oilfield pressurisation and mixing technology, which is widely used in engineering applications because of its high efficiency, durability, ability to work at high gas content, and insensitivity to solid particles such as sand (Liu et al., 2020; Deng et al., 2022; Sun et al., 2022).

In the process of crude oil and gas extraction and transportation, constrained by environmental conditions, the typical gas-liquid two-phase flow inside the transportation pipeline, the unstable flow formed by the two-phase mixing, severely tests the functional ability of the helical-axial multiphase pump, in which the problem of gas vortex clogging flow channel is particularly prominent. The phenomenon is attracting considerable critical attention from scholars in various countries. Serena and Bakken (2015), and Serena and Bakken (2016) used visualisation tests to discover that the internal flow of pumps operating at high speed is subject to shear forces, making the two-phase distribution state more uniform. While the pump operating at low-speed conditions is more likely to occur inside the 'surging' phenomenon caused by gas accumulation. Xu et al. (2019) investigated multiphase pumps' transient pressure pulsation characteristics under single-phase and gas-liquid two-phase conditions. They found that gas-liquid two-phase interaction and flow separation are the primary causes of pressure fluctuations in multiphase pumps much more significant than those in pure liquid conditions. Shi et al. (2018) used the two-fluid model (TTFM) to numerically simulate the vortex motion inside a mixed transfer pump under gas-liquid two-phase flow conditions. The results show that with the increase of inlet volume fraction, more severe flow separation, backflow, and vortex phenomena occur inside both the impeller and guide vane. From the above investigation, the thorough research of gas-liquid two-phase instability in multiphase pumps has significant engineering and theoretical significance in the optimisation design, performance improvement, and flow mechanism of multiphase pumps.

With the rapid development of computer technology (Li et al., 2022), combining experimental and numerical simulation to study the problem has become the choice of many scholars. Zhang et al. (2016a) performed non-constant computational fluid dynamics (CFD) simulations of the internal flow field of a multi-stage multiphase pump. They found that the location and characteristics of the air pockets in the impeller channel were basically consistent with the visualisation experimental results by analysing the simulation results. Yi et al. (2018) investigated the flow characteristics of a three-stage helical-axial multiphase pump using CFD numerical simulations and experimental studies. The performance variation of the multiphase pump with different bubble diameters and different interphase resistance models was investigated in detail. Suh et al. (2017) numerically analysed the flow field of multiphase pumps under different gas volume fraction (GVF) conditions based on the Eulerian-Eulerian TFM and found that GVF is an essential factor affecting the efficiency degradation and irregularity of the internal flow characteristics of multiphase pumps.

For the moment, the numerical simulation of the internal flow of multiphase pumps mainly uses the Euler-Euler TFM, which simplifies the flow in the gas-liquid two-phase flow field to a greater extent. The Euler-Euler two-fluid (TFM) ordinary particle model simplifies the gas to a sphere of equal diameter, ignoring the diameter change of bubble particles during the flow. In the actual gas-liquid two-phase flow, the bubble size inside the pump is multi-scale as the gas phase is continuously aggregated and broken. The simulation using fixed-size bubbles cannot truly reflect the flow state inside the multiphase pump. Previous studies comparing the Euler-Euler two-fluid and population balance models (PBM) have shown that the latter provides a better simulation of gas-liquid two-phase flows. Hulburt and Katz (1964) were the first to consider the problem of the non-fixed size of particles during nucleation and growth in multiphase flow simulations. They applied the moment equation to the nucleation and growth of particles and established the equilibrium equation. In the gas-liquid two-phase simulation, Lee et al. (1987) established two mathematical models of breaking and aggregation to predict

the dispersion characteristics of bubble size distribution and interface area using the PBM. The predicted results were in better agreement with the experiments. Chen et al. (2019) conducted two sets of numerical simulations of the flow field inside the electric submersible pump using a fixed size of 0.1 mm and a PBM, and the results showed that the PBM method could provide a better description of the large bubbles and gas-liquid separation phenomena within the flow field. Ge et al. (2020) used the CFD-PBM coupled model to simulate numerically and experimentally study the gas-liquid two-phase flow field of a centrifugal pump and found that the results of the CFD-PBM coupled model simulation were more similar to the experimental results by comparing with Euler-Euler TFM. Zhang et al. (2020) used CFD-PBM to investigate the two-phase distribution and the flow mechanism inside a centrifugal pump. The numerical simulation results show that CFD-PBM can accurately simulate bubbles of different sizes and find that the aggregation rate of bubbles is much larger than the rupture rate of bubbles.

This thesis will examine the way in which the Eulerian-Eulerian TFM is used as the basis, and the PBM is coupled to consider the bubble multi-size effect caused by the bubble aggregation and fragmentation phenomenon in the multiphase pump. The accuracy and reliability of the numerical simulation method are verified through experiments. The coupled TFM-PBM model was applied to study the pressure gradient force and bubble distribution characteristics of fluid microelements in the radial flow channel of the impeller. The effects of different IGVF and different flow rates on the distribution of varying bubble sizes inside the multiphase pump were analysed to reveal the gas-liquid separation phenomenon and gas stagnation behaviour inside the multiphase pump.

2 Theoretical model

2.1 Population balance model

The PBM is generally used in multiphase flows where the discrete phase has a particle size distribution (Luo, 1993; Luo and Svendsen, 1996). The population equilibrium model can describe the bubble multi-size effect caused by the bubble aggregation and fragmentation phenomenon for gas-liquid two-phase flows. Assuming that V is the volume of the particles, the transport equation of the population equilibrium model, taking into account the bubble aggregation and fragmentation is as follows:

$$\frac{\partial}{\partial t}\left[n\left[V,t\right)\right]+\nabla\cdot\left[\vec{u}n\left[V,t\right)\right]+\nabla_v\left[G_v n\left[V,t\right)\right] = B_{ag}-D_{ag}+B_{br}-D_{br} \tag{1}$$

where B_{ag} and D_{ag} are the rates of gas particle generation and death caused by aggregation, B_{br} and D_{br} are the rates of gas particle generation and death caused by fragmentation.

$$B_{ag}=\frac{1}{2}\int_0^V a(V-V',V')n(V-V',t)n(V',t)dV' \tag{2}$$

$$D_{ag}=\int_0^\infty a(V,V')n(V,t)n(V',t)dV' \tag{3}$$

$$B_{br}=\int_{\Omega_v} pg(V')\beta(V\,|\,V')n\left(V',t\right)dV' \tag{4}$$

$$D_{br}=g(V)n(V,t) \tag{5}$$

where V is the original bubble volume, V' is the sub-bubble volume, $a(V, V')$ is the bubble aggregation rate, n(V, t) is the numerical density function of the bubble, $\beta(V|V')$ is the probability density function of the bubble breaking from V' volume to volume V, $g(V)$ and is the bubble breaking rate.

2.1.1 Coalescence model

The coalescence model of Luo (1993) is used which defines the bubble aggregation rate as the product of the frequency of collision and the probability that the collision results in coalescence, with the following expression:

$$a\left(V_i,V_j\right)=\omega_{ag}\left(V_i,V_j\right)P_{ag}\left(V_i,V_j\right) \tag{6}$$

$$\omega_{ag}\left(V_i,V_j\right)=\frac{\pi}{4}\left(d_i+d_j\right)^2\bar{u}_{ij} \tag{7}$$

$$\bar{u}_{ij}=\left(\bar{u}_i^{\,2}+\bar{u}_j^{\,2}\right)^{1/2} \tag{8}$$

$$\bar{u}_{ij}=1.43(\varepsilon d_i)^{1/3} \tag{9}$$

$$P_{ag}=\exp\left\{-c_1\frac{\left[0.75\left(1+x_{ij}^2\right)\left(1+x_{ij}^3\right)\right]^{1/2}}{\left(\rho_g/\rho_l+0.5\right)^{1/2}\left(1+x_{ij}\right)^3}We_{ij}^{1/2}\right\} \tag{10}$$

$$We_{ij}=\frac{\rho_l d_i\left(\bar{u}_{ij}\right)^2}{\sigma} \tag{11}$$

where ω_{ag} is the frequency of collision, P_{ag} is the probability that the collision results in coalescence, c1 is a constant and W_{eij} is the Weber diameter.

2.1.2 Breakup model

The breakup model of Luo (1993), Luo and Svendsen (1996) is used, which considers that breakup is caused when the turbulent energy of the turbulent vortex in the gas-liquid two-phase is greater than the increment of the surface energy of the bubble after the breakup. The expression of the sub-bubble size distribution is derived directly from the bubble breakup rate function, as follows:

$$P_B\left(d,f_{BV},\lambda\right)=\exp\left[-\frac{c_f\pi d^2\sigma}{\rho_l\dfrac{4\pi}{3}\left(\dfrac{\lambda}{2}\right)^3\dfrac{\bar{u}_\lambda^{\,2}}{2}}\right] \tag{12}$$

$$P_B\left(d,f_{BV}\right)=\int_{\lambda\min}^{d}P_B(d,f_{BV},\lambda)\bar{\omega}_{B,\lambda}(d,\lambda)d\lambda,\lambda_{\min}=0.2d \tag{13}$$

$$P_B(d)=\frac{1}{2}\int_0^1 P_B\left(d,f_{BV}\right)df_{BV},b(V')=P_B(b)/n_d \tag{14}$$

$$\bar{\omega}_{B,\lambda}(d,\lambda)=\frac{\pi}{4}(d+\lambda)^2\bar{u}_\lambda\dot{n}_\lambda n_d \tag{15}$$

$$\dot{n}_\lambda=\frac{0.822(1-\alpha)}{\lambda^4} \tag{16}$$

$$\beta(V\mid V')=\frac{P_B(d,f_{BV})}{P_B(d)} \tag{17}$$

where f_{BV} is the volume ratio of the sub-bubble to the original bubble after bubble breakage, $P_B(d, F_{BV}, \lambda)$ is the probability that the turbulent energy can cause bubble f_{BV} breakage for a turbulent vortex size of λ, $P_B(d, f_{BV})$ is the frequency of bubble V' to undergo f_{BV} breakup for a range of turbulent vortex sizes $[\lambda_{min}, d]$ where energy exists that can cause bubble f_{BV} breakup, $P_B(d)$ represents the frequency of arbitrary fragmentation of bubble V' within the range of turbulent vortex sizes $[\lambda_{min}, d]$ that can cause f_{BV} fragmentation, $\bar{\omega}_{B,\lambda}(d,\lambda)$ is the average frequency of collision between a bubble of diameter d and a turbulent vortex of size λ in a unit volume, $\dot{n}_\lambda$ is the number density of turbulent vortices of size λ to $\lambda + d_\lambda$, and $\beta(V|V')$ is the probability of generating sub-bubbles V after the breakup of bubble V'.

Then the bubble breakup probability is

$$\beta(V\mid V')b(V')=P_B(d,f_{BV})/n_d \tag{18}$$

3 Physical model and numerical methods

3.1 Geometric model

For the convenience and accuracy of the numerical study, a single compression unit of the helical-axial multiphase pump is selected as the object of study in this paper, and the main performance parameters of the multiphase pump are shown in Table 1. The compression unit comprises an inlet section, impeller, guide vane, and outlet section; the main geometric parameters of the impeller and guide vane are shown in Table 2.

Table 1 The performance geometric parameters of the multiphase pump

Parameter	*Numerical value*
Design flow rate Q_d/(m^3/h)	100
Head H/m	30
Rotational speed n/(r/m)	4,500
Efficiency η/%	62

3.2 Meshing and independence verification

ICEM CFD and TurboGrid software are used to structure the calculation domain for meshing. Considering the complex surface shape of the impeller and guide vanes, they are locally encrypted, and the boundary layer is arranged near the wall surface (y + < 40) (Yang et al., 2022; Peng et al., 2022). The calculation domain mesh is shown in Figure 1. To avoid the influence of the number of grids on the calculation results, the grid independence is judged by the standard of the head reaching a stable value at 30% of the design flow rate and inlet gas content and the head variation of Case 5 and 6 is less than 0.5%, as shown in Figure 2. Case 5 is selected for the numerical calculation of the multiphase pump with comprehensive consideration of calculation resources and accuracy.

Table 2 Main parameters of the hydraulic parts of a multiphase pump

Hydraulic parts	*Main structural parameter*	*Value*
Impeller	Diameter D/(mm)	150
	Number of blades Z	4
	Axial length e/(mm)	55
	Half cone angle of the hub γ(◦)	6
	Inlet angle of the blade β_1	10
	Outlet angle of the blade β_2	14
Guide vane	Diameter D_d/(mm)	150
	Number of blades Z_d	17
	Axial length e_d/(mm)	55
	Half cone angle of the hub γ(◦)	6
	Inlet angle of the blade β_{d1}	38
	Outlet angle of the blade βd_2	90

Figure 1 Computational domain and mesh (see online version for colours)

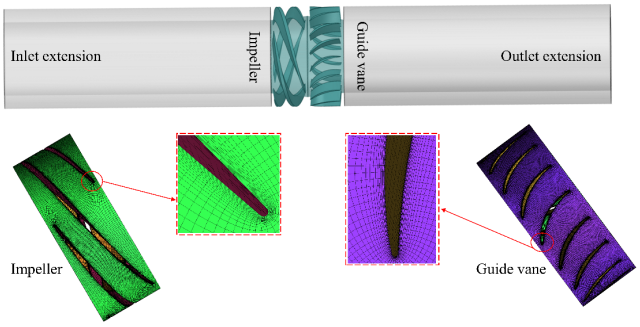

3.3 Numerical solution setting

An important parameter affecting the flow mechanism inside the pump is the bubble size db. It is known that the bubble diameter inside the multiphase pump is in the range of 0.1–10 mm and has a normal distribution relationship with the number of bubbles, according to the visualisation test results of Zhang et al. (2016b, 2018). The governing equations are discretised using the finite volume method. A high-resolution scheme is employed for the convection terms, and in unsteady simulations, the temporal terms are discretised using a second-order backward Euler method. This paper employs ANSYS FLUENT (Landvogt et al., 2014) for the CFD-PBM coupled simulations inside the multiphase pump. 10 groups of discrete bubble sizes were used to study the bubble coalescence and breakup mechanism within the pump, and the detailed bubble size

range is shown in Table 3. Water and air are chosen as the flow media, the SST k-ω turbulence model is used for the liquid phase, and the zero-equation turbulence model is used for the gas phase (Han et al., 2020).

Figure 2 Mesh independence verification (see online version for colours)

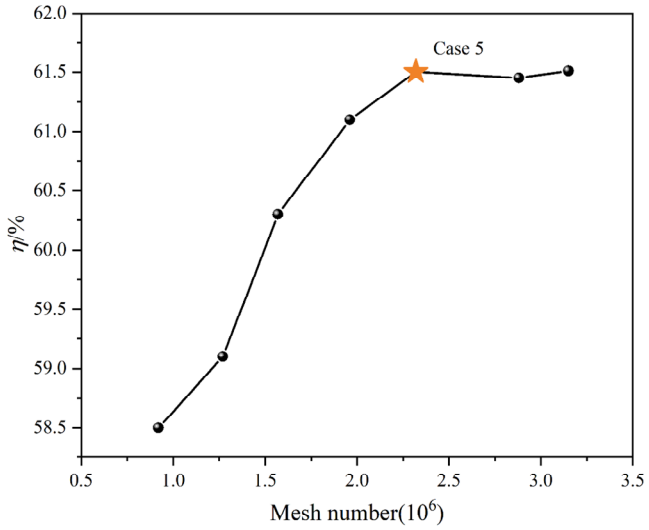

The SST k-ω model takes into account the shear stress transport effect and can effectively capture the flow separation. The solution method is set as phase coupled simple method, the no-slip boundary condition is adopted for solid walls, and the convergence accuracy is set to 10^{-5}.

Table 3 PBM discrete bubble sizes

Air bubble group (db)	*Diameter/mm*
d0	10.00
d1	5.99
d2	3.59
d3	2.15
d4	1.29
d5	0.77
d6	0.46
d7	0.28
d8	0.17
d9	0.10

First, based on the Eulerian-Eulerian multiphase flow model, steady-state calculations are performed for the multiphase pump. The inlet and outlet boundary conditions are set as velocity inlet and pressure outlet, respectively. The inlet velocity is calculated based on the desired flow rate and the GVF is specified at the inlet. Turbulent boundary conditions for the liquid phase at the inlet are set by providing turbulent intensity and hydraulic diameter, with the turbulent intensity set at a moderate level (5%) and the hydraulic diameter at 150 mm. The initial flow fields in the rotating region (impeller) and stationary region are computed using the multiple reference frame (MRF) approach, and numerical transfer at the cross interface is conducted through nodal interpolation. Once the steady-state calculations have reached stability, the unsteady flow field is obtained by coupling the PBM model and transient terms and replacing MRF with a sliding mesh approach for both the stationary and rotating regions. Additionally, moderate bubble sizes d_3 and d_4 are selected as the bubble sizes at the inlet of the multiphase pump (Chen et al., 2019), while the remaining inlet boundary conditions are kept consistent with the steady-state calculations. The transient calculation time step is required for every 3° of impeller rotation, which is 1.68×10^{-4} s. The total time is the time needed for 8 cycles of impeller rotation.

Figure 3 Gas-liquid two-phase flow pump performance test bench (a) the schematic diagram of the gas-liquid two-phase flow pump performance test bench, 1,4,15,16,18-pressure gauge; 2-electromagnetic flowmeter; 3-liquid inlet valve; 5-low pressure tank; 6-gas valve; 7-air compressor; 8-air compressor control room; 9-flowmeter; 10-gas inlet valve; 11-electromotor; 12-coupling; 13-torque sensor; 14-model pump; 17-medium pressure tank (b) picture of the test bench (see online version for colours)

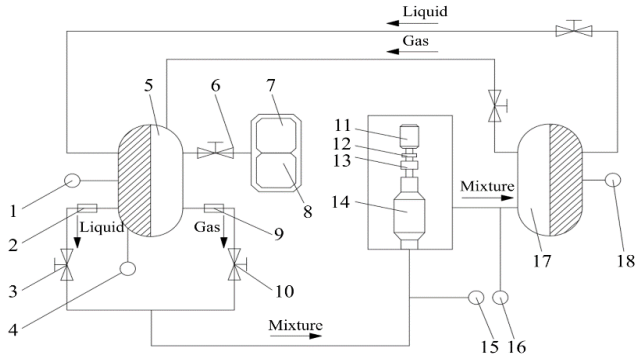

(a)

(b)

3.4 *Experimental validation*

Figure 3 shows the schematic diagram of the multiphase pump test system. The test system is mainly composed of the multiphase pump, variable frequency motor, speed torque meter, air compressor, liquid regulating valve, gas regulating valve and flow meter, import and export pressure transmitter, etc. The air compressor pressurises the gas during the test, the liquid regulating valve controls the liquid flow, and the gas regulating valve controls the gas flow into the pipeline. The relevant parameters, including

pressure, flow rate, gas content rate, and shaft power, were obtained through the corresponding measuring devices to obtain the external characteristic curves of multiphase pumps under different working conditions.

The head and efficiency at different flow rates obtained by numerical simulation for IGVF = 30% are compared with the experimental results, as shown in Figure 4. As can be seen from the figure, the performance curves obtained from the numerical simulations have the same trend as the experimental curves. However, the numerical simulation did the mechanical and volumetric losses without considering them, resulting in some errors with the experimental results, with the maximum head error of 7.1% and the maximum efficiency error of 9.1%. The mistakes of head and efficiency are 4.7% and 6.1% at the design working condition. Therefore, the numerical simulation method and grid model used in this paper have certain reliability.

Figure 4 Comparison between numerical simulation external characteristics and experimental external characteristics of the multiphase pump (see online version for colours)

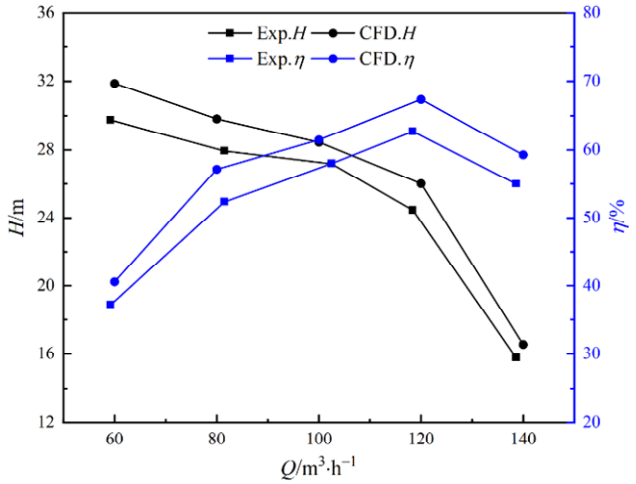

4 Analysis of results

4.1 Analysis of the air-blocking mechanism

Figure 5 illustrates the gas flow line distribution at the hub of the impeller for one rotation cycle when IGVF = 30%, from which the vortex distribution at the hub of each impeller channel can be observed. After experiencing a rotation cycle, the vortex remains in the impeller channel. The congregation of air almost the entire channel outlet causes the phenomenon of 'air blockage'; the gas distribution in different flow channels of the impeller is different and inhomogeneous.

Because the multiphase pump is in the process of working, the flow of gas and liquid in the flow channel under the action of different centrifugal forces produces flow separation so that the uneven flow of gas to form a gas stagnation vortex group hinders the normal movement of the fluid. Gas stagnation in the impeller channel significantly reduces the fluid flow area, which in turn makes the relative velocity of the liquid phase increase, resulting in excessive flow losses that reduce the hydraulic performance of the pump. Extreme pressure at the gas blockage may lead to a 'water hammer' effect, threatening the safety of the entire mixing system and the pump. Therefore, it is necessary to further analyse the phenomenon of gas-liquid separation in the multiphase pump.

Figure 5 Impeller and guide vane flow path hub at the gas content and gas flow line distribution (see online version for colours)

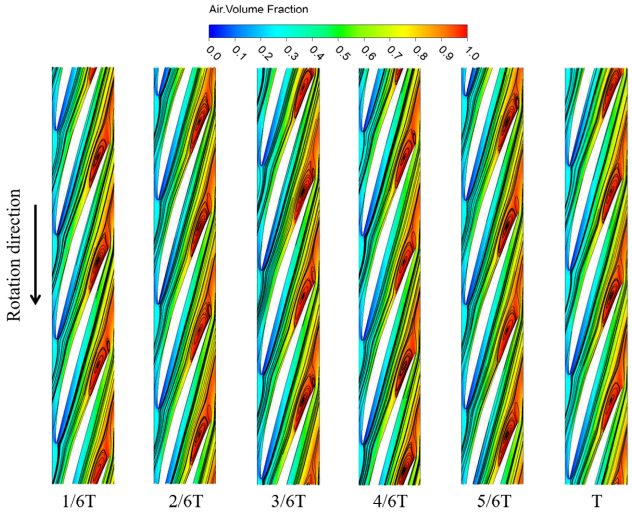

Figure 6 Schematic diagram of the impeller meridian surface (see online version for colours)

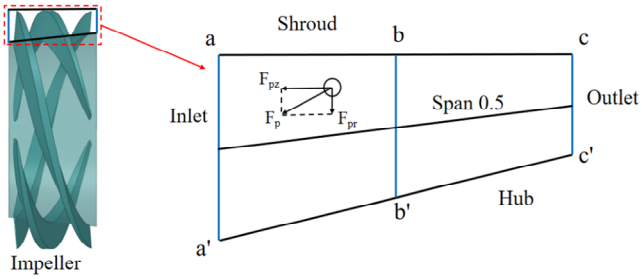

Figure 7 Radial pressure difference curve of impeller channel at different IGVF (see online version for colours)

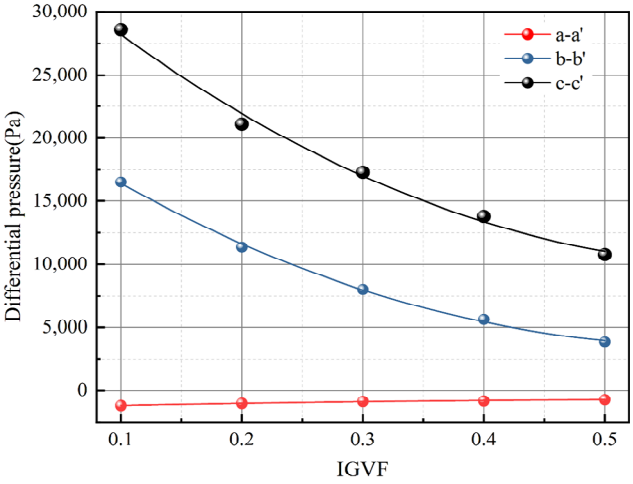

An in-depth analysis of the pressure gradient forces on the fluid microelements can reveal the mechanism of gas-liquid separation inside the multiphase pump. Figure 6 shows a schematic diagram of the impeller meridian surface, in which a-a represents the inlet position of the channel, b-b′ represents the middle position of the channel, and c-c′ represents the outlet position of the channel.

Figure 8 Variation curve of the pressure difference between the blade heights at different positions of the impeller channel (see online version for colours)

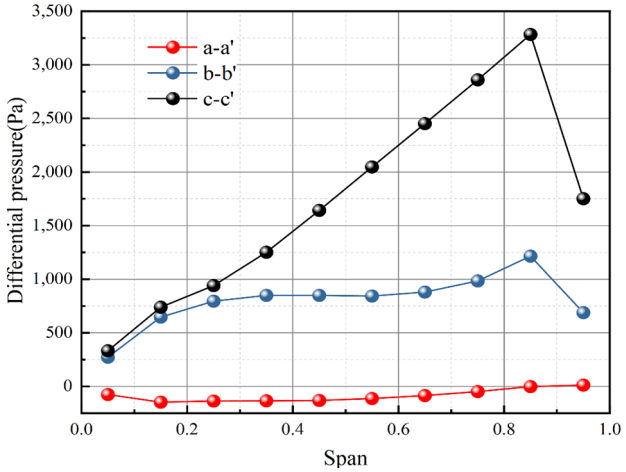

Figure 9 Radial bubble diameter distribution curve of impeller channel at different IGVF (see online version for colours)

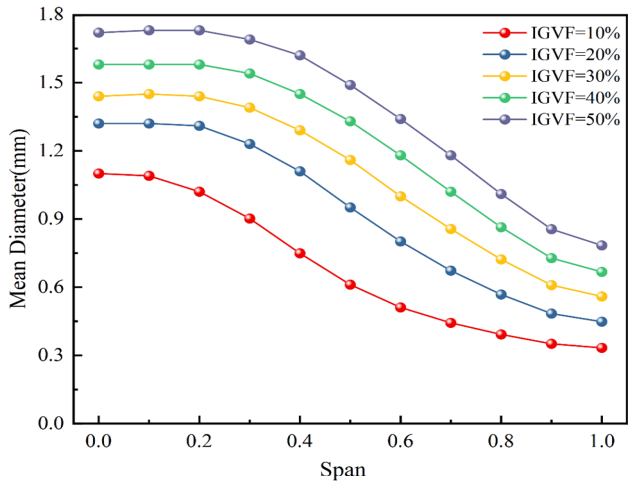

The variation of the differential pressure between the impeller shroud and hub at different IGVFs is shown in Figure 7. When the IGVF increases, the pressure difference curve is relatively flat at the impeller inlet a-a′, and the pressure gradient force generated by the pressure difference has minimal effect on the gas-liquid separation; The pressure difference at the impeller channel b-b′ and the impeller outlet c-c′ is obviously declining. That is to say, from the middle of the impeller channel to the outlet, the radial pressure gradient force generated by the impeller rotation does not provide enough centripetal force to the liquid. And provides excess centripetal force to the gas so that both gas and liquid phases cannot maintain equilibrium, and the gas and liquid phases move in opposite directions in the radial direction, resulting in the phase separation of gas and liquid phases.

The pressure difference variation curves between the blade heights at different locations of the impeller channel are shown in Figure 8. The pressure difference between different blade heights at a-a' shows a slight fluctuation, the pressure difference is insignificant, and the gas-liquid phase separation is not apparent. The pressure difference between different blade heights at b-b′ shows a sizeable upward slope trend at the hub side, which proves that the pressure difference is enormous and the gas-liquid separation at the hub side is severe. The pressure difference between different blade heights at c-c′ tends to rise first and then decline because the impeller shroud is filled with liquid here, and the hub is filled with gas. The pressure difference between the shroud and the hub changes markedly, and the gas-liquid two-phase separation is profound.

Figure 9 shows the bubble diameter distribution curves from the hub to the rim at the impeller exit position (c-c) under different IGVF. From the figure, it can be clearly observed that the average bubble diameter at different IGVF from the hub to the rim of the impeller shows a decreasing characteristic. The bubble mean diameter at the hub is much larger than that at the shroud; This trend indicates that the aggregation and distribution range of the gas phase has an influence on the bubble diameter, and the bubble diameter is more prominent where the gas phase aggregation is severe. The logistic function was used to fit the functional relationship between the bubble mean diameter (d) and the different leaf height positions at the impeller outlet (x). The correlation function is shown in equation (19).

$$d = 0.5\alpha + 0.2 + \frac{\alpha + 0.8}{1 + \left(\dfrac{x}{-1.9\alpha^2 + 1.85\alpha + 0.3}\right)^3} \tag{19}$$

where α is the inlet gas volume fractions (IGVF).

4.2 *Bubble distribution law for different IGVF*

Figure 10 demonstrates the distribution of mean bubble diameter in a multiphase pump at different IGVFs. The mean bubble size was much bigger than the other regions at the impeller inlet. The bubbles had not yet undergone the bubble coalescence and breakup movement at this time. After entering the impeller in a rotating state of the fluid, the overall mean bubble size under the action of shear force is a strong downward trend, indicating that the frequency of bubble breakup in the flow channel at this time is much greater than the frequency of bubble coalescence. Large bubbles are broken into small bubbles and then blended with the liquid into a homogeneous gas-liquid two-phase flow. In addition, as the increase of IGVF makes the gas-liquid two-phase interaction obvious, the flow within the impeller is also more turbulent. It can be seen from Figure 10 that the average bubble size at different flow path positions increases overall with the increase of IGVF, and the frequency of bubble agglomeration in the impeller

increases at this time. The interaction between the gas and liquid phases in the flow channel is more pronounced.

According to the graph of the bubble size percentage inside the impeller and guide vane shown in Figure 11, what emerges from the results from the chart here is that the curves are parabolic at different gas content rates. The initial size of the bubble at the impeller inlet is 1.03 mm; when the bubble diameter is less than 1.03 mm, the bubble in the flow channel undergoes breakup movement. Conversely, the bubble in the flow channel is considered to be experiencing coalescence behaviour. In low inlet gas content conditions, bubbles tend to break up from large to small bubbles. In contrast, the percentage of large-size bubbles gradually increases with the increase of IGVF; the small-size bubbles keep gathering and merging into large-size bubbles. Figure 12 shows the gas distribution in the impeller and guide vane channel at different IGVF. The gas morphology is represented by the 80% GVF isometric diagrams, and the mean bubble diameter is used to colour the gas to visualise the gas distribution and aggregation in the pump channel at different IGVF. Combined with Figure 11, it can be seen that the degree of gas accumulation in the flow channel is positively correlated with IGVF. When the gas content is as high as 50%, the proportion of large-sized bubbles is the highest, and the degree of gas accumulation in the flow channel is also the most severe; this suggests that large bubbles are more likely to be trapped in the impeller and lead to the turbulent flow state.

Figure 10 The mean bubble diameter distribution curve of the impeller and guide vane under different IGVF (see online version for colours)

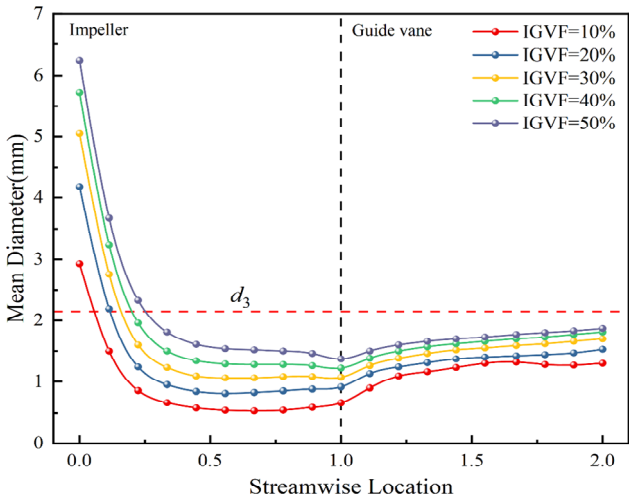

According to the correlational of figure analysis can be seen the proportion of bubbles of each size in the guide vane flow channel varies with IGVF in the same trend as the guide vane flow channel. The proportion of d_0–d_1 bubbles inside the guide vane is lower than that of bubbles inside the impeller. However, the proportion of d_2–d_4 bubbles is significantly higher than that of bubbles inside the impeller. Because of the pressure expansion effect of the guide vane, the gas-liquid phase in the flow channel is relatively balanced; therefore, the gas phase is relatively uniformly distributed in the guide vane flow path.

4.3 Bubble distribution law for different flow rate

Figure 13 shows that when IGVF = 30%, the impeller's mean bubble diameter distribution curves and guide vane flow channels at different flow rates. Figure 14 shows the gas distribution in the impeller and guide vane channel at different flow rates. The gas morphology is represented by the 80% GVF isometric diagrams, and the mean bubble diameter is used to colour the gas to visualise the gas distribution and aggregation in the pump channel at different flow rates. Combining the two figures, it can be seen that the mean bubble diameter from the impeller inlet to the middle flow path of the impeller increases as the flow rate continues to grow. The mean bubble diameter from the middle channel of the impeller to the outlet of the impeller is on a descending trend, indicating that the capacity of the liquid to carry the gas under a high flow rate and the resistance effect of the liquid on the gas are enhanced, making it increasingly difficult to gather bubbles. In addition, the different states of the fluid in the impeller and guide vane also affect the breakup and coalescence movement of the bubbles in the flow channel. When the impeller is operating, the bubbles in the flow channel will be continuously broken by the rotating effect, which decreases the bubbles' average diameter.

Figure 11 Bubble size proportion in the impeller and guide vane at different IGVF (see online version for colours)

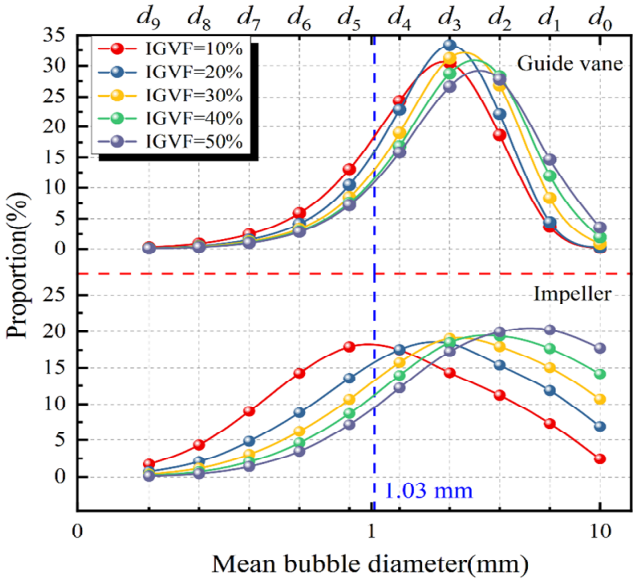

In the guide vane, the fluid including bubbles in a relatively static state; the bubbles are not subjected to external forces of shear, resulting in the bubbles in the guide vane flow channel tending to occur in coalescence movement, making the mean bubble diameter higher than the impeller flow channel. At the guide vane outlet, the relationship between the size of the average bubble diameter at different operating conditions corresponds to the gas accumulation in the channel in Figure 14. The mean bubble diameter is the

largest at the design flow condition when the gas accumulation in the flow channel is the most severe, followed by the 1.2–1.4 Q_d condition and the smallest at the 0.6–0.8 Q_d condition, as shown in the red box in Figure 13. As the fluid flow in the vane is influenced by the state of the fluid at the impeller outlet at operating conditions of 0.6–0.8 Q_d, the gas in the impeller channel has the most significant accumulation. The liquid has the least ability to carry the gas, so the gas in the vane accumulates to a lesser extent. In 1.2–1.4 Q_d conditions, the gas accumulation and gas phase vortex in the flow channel are mitigated because the fluid has sizeable kinetic energy at high flow conditions.

Figure 12 Gas distribution in the impeller and guide vane at different IGVF (see online version for colours)

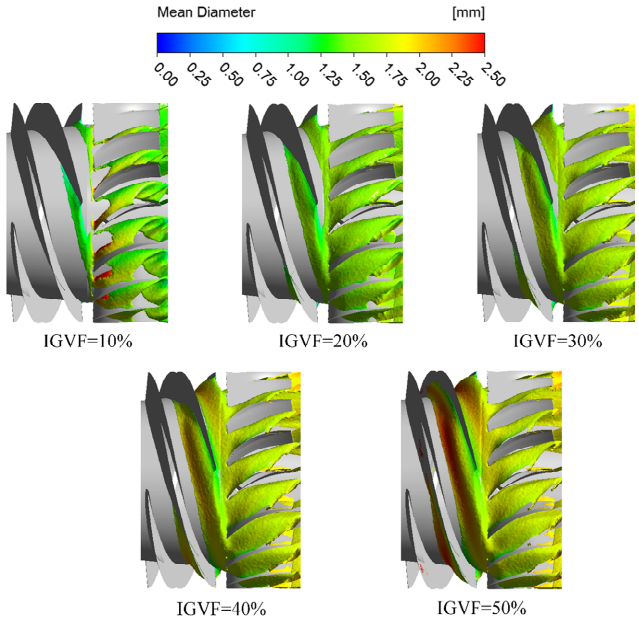

Figure 13 The mean bubble diameter distribution curve of the impeller and guide vane under different flow rates (see online version for colours)

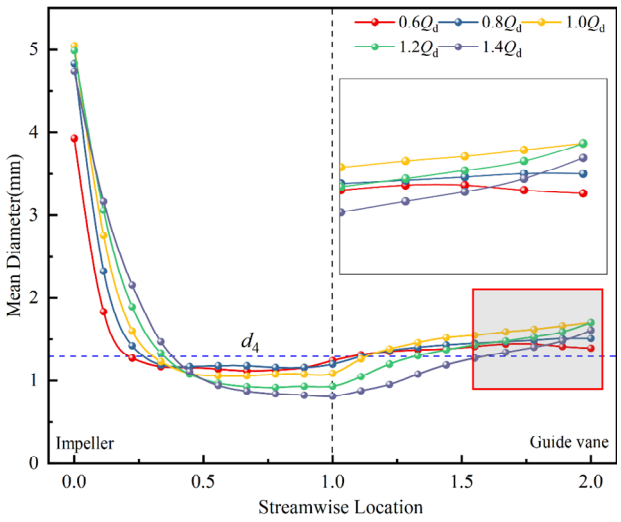

Figure 14 Gas distribution in the impeller and guide vane at different flow rates (see online version for colours)

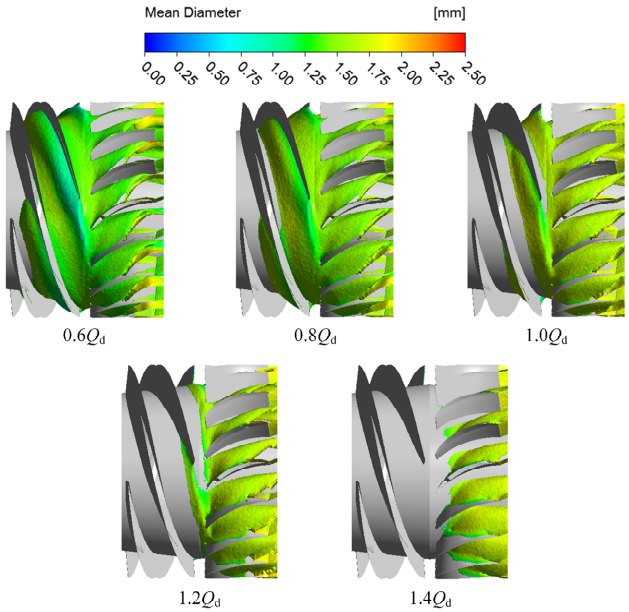

5 Conclusions

In this paper, by considering the bubble multi-size problem caused by bubble coalescence and breakup motion in the flow field of the multiphase pump, the size distribution characteristics of bubbles under different motion parameters are analysed by applying the coupled TFM-PBM model. The analysis results are as follows:

1 Gas-liquid separation significantly affects gas mass stagnation and flow instability in the internal flow field of multiphase pumps. A detailed analysis of the influence of axial and radial pressure gradient forces on different fluid microelements reveals that the impeller outlet, specifically against the hub, experiences the most significant pressure difference changes, leading to profound gas-liquid two-phase separation. Furthermore, at different IGVF, the bubble size on the hub side is much larger than that on the shroud side, which indicates continuous clustering and movement of bubbles, resulting in the formation of large air mass vortices at the hub measurement.

2 The findings of this study demonstrate that the IGVF has a substantial impact on bubble size within the flow channel. At lower IGVF, bubbles tend to undergo bubble breakup motion, while at higher IGVF, they tend to aggregate. When the IGVF reaches 50%, there is the highest proportion of large-size bubbles with d_0–d_2 diameter in the impeller, and the degree of aggregation at the impeller outlet hub-side is also the most severe during this time.

3 The average bubble size under varying flow conditions is closely associated with the extent of gas aggregation. As the flow rate increases, its ability to carry gas also increases, leading to a decrease in both the average

bubble size and the degree of aggregation within the impeller. The flow state within the guide vane is influenced by the flow within the impeller; the size relationship is 1.0 Q_d > 1.2–1.4 Q_d > 0.6–0.8 Q_d. The bubble size at different flow rates corresponds to the degree of gas aggregation.

Acknowledgements

This study was supported by The National Natural Science Foundation of China (52269022,52179086), Key Technology Research of Large-Scale Stepped Pumping Station Renovation of Jingtai River Electricity Irrigation Project (2020-70), and The Innovation Star Project of Gansu Province (2023CXZX-436).

References

Chen, Y., Patil, A., Chen, Y., Bai, C., Wang, Y. and Morrison, G. (2019) 'Numerical study on the first stage head degradation in an electrical submersible pump with population balance model', *Journal of Energy Resources Technology*, Vol. 141, No. 2, pp.022003.1–022003.11.

Deng, Y., Wang, X., Xu, J., Li, Y., Zhang, Y. and Kuang, C. (2022) 'Gas–liquid interaction characteristics in a multiphase pump under different working conditions', *Processes*, Vol. 10, No. 10, p.1977.

Ge, Z., He, D., Huang, R. et al. (2020) 'Application of CFD-PBM coupling model for analysis of gas-liquid distribution characteristics in centrifugal pump', *Journal of Petroleum Science and Engineering*, Vol. 194, p.107518.

Han, W., Li, X., Su, Y., Su, M., Li, R. and Zhao, Y. (2020) 'Effect of thickness ratio coefficient on the mixture transportation characteristics of helical-axial multiphase pumps', *Applied Sciences*, Vol. 10, No. 1, p.345.

Hulburt, H.M. and Katz, S. (1964) 'Some problems in particle technology: a statistical mechanical formulation', *Chemical Engineering Science*, Vol. 19, No. 8, pp.555–574.

Landvogt, B., Osiecki, L., Patrosz, P. et al. (2014) 'Numerical simulation of fluid-structure interaction in the design process for a new axial hydraulic pump', *Progress in Computational Fluid Dynamics, an International Journal*, Vol. 14, No. 1, pp.31–37.

Lee, C.H., Erickson, L.E. and Glasgow, L.A. (1987) 'Bubble breakup and coalescence in turbulent gas-liquid dispersions', *Chemical Engineering Communications*, Vol. 59, Nos. 1–6, pp.65–84.

Li, W., Li, Z., Han, W. et al. (2023) 'Measured viscosity characteristics of Fe3O4 ferrofluid in magnetic and thermal fields', *Physics of Fluids*, Vol. 35, No. 1, p.12002.

Li, W., Li, Z., Qin, Z. et al. (2022) 'Influence of the solution pH on the design of a hydro-mechanical magneto-hydraulic sealing device', *Engineering Failure Analysis*, Vol. 135, p.106091

Liu, M., Tan, L. and Cao, S. (2020) 'Method of dynamic mode decomposition and reconstruction with application to a three-stage multiphase pump', *Energy*, Vol. 208, p.118343.

Luo, H. (1993) *Coalescence, Breakup and Liquid Circulation in Bubble Column Reactors*, The University of Trondheim, Trondheim.

Luo, H. and Svendsen, H.F. (1996) 'Theoretical model for drop and bubble breakup in turbulent dispersions', *AIChE Journal*, Vol. 42, No. 5, pp.1225–1233.

Peng, C., Zhang, X., Gao, Z., Wu, J. and Gong, Y. (2022) 'Research on cooperative optimization of multiphase pump impeller and diffuser based on adaptive refined response surface method', *Advances in Mechanical Engineering*, Vol. 14, No. 1, p.16878140211072944.

Serena, A. and Bakken, L.E. (2015) 'Design of a multiphase pump test laboratory allowing to perform flow visualization and instability analysis', *Housing Studies*, Vol. 23, No. 6, pp.857–878.

Serena, A. and Bakken, L.E. (2016) 'Flow visualization of unsteady and transient phenomena in a mixed-flow multiphase pump', *ASME Turbo Expo: Turbomachinery Technical Conference and Exposition.*

Shi, G.T., Wang, Z.W., Luo, K. et al. (2018) 'Effect of gas volume fraction on the vortex motion within the oil-gas multiphase pump', *IOP Conference Series: Earth and Environmental Science*, IOP Publishing, Vol. 163, No. 1, p.12002.

Suh, J-W. et al. (2017) 'A study on numerical optimization and performance verification of multiphase pump for offshore plant', *Proceedings of the Institution of Mechanical Engineers, Part A: Journal of Power and Energy*, Vol. 231, No. 5, pp.382–397.

Sun, W., Yu, Z., Zhang, K. and Liu, Z. (2022) 'Analysis of tip clearance effect on the transportation characteristics of a multiphase rotodynamic pump based on the non-uniform bubble model', Fluids, Vol. 7, No. 2, p.58.

Wangxu, L., Zhenggui, L., Wanquan, D. et al. (2021) 'Particle image velocimetry flowmeter for natural gas applications', *Flow Measurement and Instrumentation*, Vol. 82, No. 82, p.102072.

Xu, Y., Cao, S., Sano, T. et al. (2019) 'Experimental investigation on transient pressure characteristics in a helical-axial multiphase pump', *Energies*, Vol. 12, No. 3, p.461.

Yang, S.S., Fang, T., Wang, T. et al. (2022) 'Value of blade number in centrifugal flow pumps in both turbine and pump mode through experimental and numerical means', *Progress in Computational Fluid Dynamics, an International Journal*, Vol. 22, No. 4, pp.197–218.

Yi, S. et al. (2018) 'Experiment and numerical study of a new generation three-stage multiphase pump', *Journal of Petroleum Science and Engineering*, Vol. 169, pp.471–484.

Zhang, F., Zhu, L., Chen, K., Yan, W., Appiah, D. and Hu, B. (2020) 'Numerical simulation of gas–liquid two-phase flow characteristics of centrifugal pump based on the CFD–PBM', *Mathematics,* Vol. 8, p.769, https://doi.org/10.3390/math8050769.

Zhang, J. et al. (2016a) 'Visualization study of gas-liquid two-phase flow patterns inside a three-stage rotodynamic multiphase pump', *Exp. Therm. Fluid Sci.*, Vol. 70, pp.125–138.

Zhang, J., Li, Y., Cai, S. et al. (2016b) 'Investigation of gas-liquid two-phase flow in a three-stage rotodynamic multiphase pump via numerical simulation and visualization experiment', *Advances in Mechanical Engineering*, Vol. 8, No. 4, DOI: 1687814016642669.

Zhang, J. et al. (2018) 'An investigation of the flow characteristics of multistage multiphase pumps', *Int. J. Numer. Methods Heat Fluid Flow*, Vol. 28, No. 3, pp.763–784.